Entanglement Generation in Superconducting Qubits Using Holonomic Operations

D.J. Egger, M. Ganzhorn, G. Salis, A. Fuhrer, P. Müller, P.Kl. Barkoutsos, N. Moll, I. Tavernelli, and S. Filipp

Entanglement generation in superconducting qubits using holonomic operations

D. J. Egger, M. Ganzhorn, G. Salis, A. Fuhrer, P. Müller, P. Kl. Barkoutsos, N. Moll, I. Tavernelli, and S. Filipp

IBM Research GmbH, Zurich Research Laboratory, Säumerstrasse 4, 8803 Rüschlikon, Switzerland

(Dated: December 13, 2018)

We investigate a non-adiabatic holonomic operation that enables us to entangle two fixed-frequency superconducting transmon qubits attached to a common bus resonator. Two coherent microwave tones are applied simultaneously to the two qubits and drive transitions between the first excited resonator state and the second excited state of each qubit. The cyclic evolution within this effective 3-level Λ-system gives rise to a holonomic operation entangling the two qubits. Two-qubit states with 95% fidelity, limited mainly by charge-noise of the current device, are created within 213 ns. This scheme is a step toward implementing a SWAP-type gate directly in an all-microwave controlled hardware platform. By extending the available set of two-qubit operations in the fixed-frequency qubit architecture, the proposed scheme may find applications in near-term quantum applications using variational algorithms to efficiently create problem-specific trial states. We illustrate this point by computing the ground state of molecular hydrogen using the holonomic operation.

I. INTRODUCTION

Superconducting qubits are one of the leading candidates to build a quantum computer [1]. They are fabricated with conventional micro- and nanofabrication techniques [2, 3] and are controlled using standard microwave instrumentation. The fixed-frequency transmon is a specific version of a superconducting qubit that is not sensitive to flux [4]. This improves the qubit coherence time at the cost of controllability. Fixed-frequency qubits can be coupled dispersively through coupling elements such as coplanar wave-guide resonators [5, 6]. Two-qubit operations are then activated by applying coherent microwave signals to generate, e.g., a controlled-NOT operation using the cross-resonance gate [7, 8].

In this paper we demonstrate an alternative all-microwave entangling scheme in which we simultaneously drive transitions between a resonator and two fixed-frequency qubits [9]. This scheme is based on a holonomy emerging in a driven Λ-type system with three energy levels [10–19]. Such quantum operations have attracted attention because they may be exploited for holonomic quantum computing based on non-abelian geometric phases created by steering the system along a closed loop in Hilbert space [20, 21]. Holonomic quantum computing may benefit from the robustness of geometric phases to certain types of errors [22–34]. While in theory, holonomic adiabatic gates can reach high fidelities in the limit of long gate duration [34, 35], decoherence in real devices severely limits the achievable gate fidelities. A particular challenge is to realize holonomic two-qubit operations. A few experimental demonstrations exist but operate either on different degrees of freedom [36] or use a trotterized approach [37]. Here, we present a direct realization of a non-adiabatic two-qubit holonomic operation that entangles two superconducting qubits in a scalable architecture [38]. Furthermore, the holonomic operation does not constrain the qubit frequencies as much as the cross-resonance gate does. Moreover, in contrast to the cross-resonance gate which realizes a CNOT primitive, the holonomy results in an exchange-type operation which may be useful to reduce the circuit depth in various quantum algorithms [39]. As a benchmark test, we compute the energy of the ground state of molecular hydrogen using the holonomy.

This paper is structured as follows. Section II introduces the holonomic operation and the experimental setup. Section III discusses the various steps needed to calibrate the holonomic operation. Experimental results and simulations are discussed in sections IV and V, respectively. The experimental determination of the energy of the ground state of molecular hydrogen is shown in section VI.

II. SETUP AND HOLONOMIC OPERATION

The system is made up of two fixed-frequency superconducting qubits coupled to a common coplanar wave-guide resonator, see Fig. 1(a). The coupling strengths are $g_1/(2\pi) = 156$ MHz and $g_2/(2\pi) = 196$ MHz and the resonator frequency is $\omega_r/(2\pi) = 6.272$ GHz. The Hamiltonian describing the system is

$$\hat{H} = \omega_r \hat{a}^\dagger \hat{a} + \sum_{i=1,2} \omega_i \hat{b}_i^\dagger \hat{b}_i + \frac{\alpha_i}{2} \hat{b}_i^\dagger \hat{b}_i^\dagger \hat{b}_i \hat{b}_i$$
$$+ g_i \left(\hat{b}_i^\dagger \hat{a} + \hat{b}_i \hat{a}^\dagger \right) + \Omega_i(t) \left(\hat{b}_i^\dagger + \hat{b}_i \right). \quad (1)$$

Here $\hbar = 1$, $\hat{b}_i$ ($\hat{b}_i^\dagger$) is the lowering (raising) operator of qubit i whilst $\hat{a}$ ($\hat{a}^\dagger$) is the resonator lowering (raising) operator. The qubit frequencies and anharmonicities are $\omega_1/(2\pi) = 4.896$ GHz and $\omega_2/(2\pi) = 4.689$ GHz and $\alpha_1/(2\pi) = -330$ MHz and $\alpha_2/(2\pi) = -333$ MHz, respectively. The system is operated in the dispersive regime $|\Delta_i| = |\omega_i - \omega_r| \gg g_i$ to avoid direct qubit-resonator excitation transfer. The T_1 times of qubit one (Q1), qubit two (Q2) and the coupling resonator are 42 μs, 56 μs and 7 μs, respectively. Each qubit is driven by a microwave signal with a time-dependent amplitude $\Omega_i(t)$ applied via individual capacitively coupled charge bias lines.
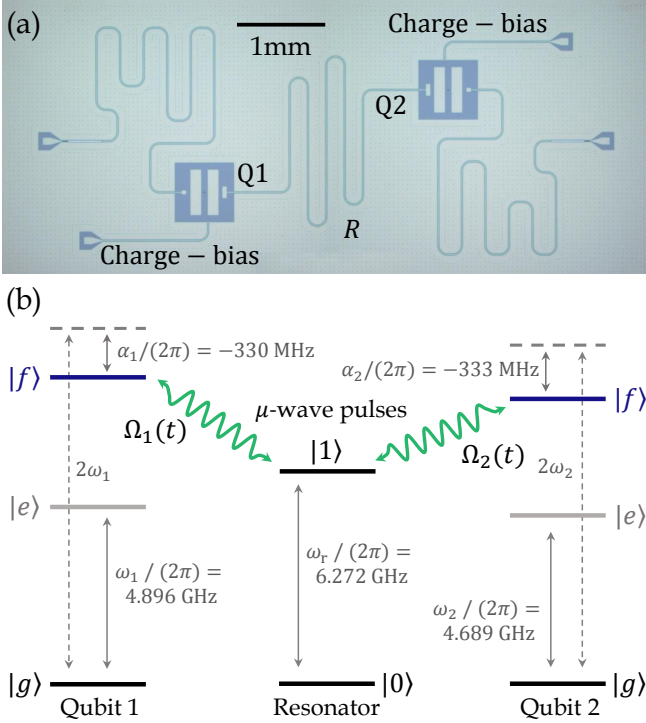
Figure 1. (a) Micrograph of the superconducting qubit chip with two transmons (Q1 and Q2) connected via a coplanar wave-guide resonator (R). The transmon-style qubits are individually addressed through capacitively coupled charge-bias lines and measured using coplanar wave-guide readout resonators. (b) Level diagram of the two qubits with energy levels $|g\rangle$, $|e\rangle$ and $|f\rangle$ connected to a resonator with lowest lying states $|0\rangle$ and $|1\rangle$. The holonomic operation is created by microwave drives $\Omega_{1,2}(t)$ between the $|f\rangle$ state of each qubit and the $|1\rangle$ state of the resonator.

Entanglement with holonomic operations

In our experiments we use the first three transmon states $|g\rangle$, $|e\rangle$ and $|f\rangle$, here listed in order of increasing energy. The two-qubit operation described in this paper is realized by simultaneously driving the $|f0\rangle$ to $|g1\rangle$ transition of each qubit where $|0\rangle$ is the ground state and $|1\rangle$ is the excited state of the resonator, see Fig. 1(b). These qubit-resonator transitions, as well as the single qubit transitions, are controlled by applying the microwave drive $\Omega_i(t) = \lambda_i \eta_i(t) \cos(\omega_{d,i} t + \varphi_i)$ with adjustable frequency $\omega_{d,i}$, phase φ_i, and pulse envelope $\eta_i(t)$ to each qubit. The complex scalars λ_i are the relevant scaling factors for the two-qubit holonomic operation.

Applying a drive on qubit i at frequency $\omega_{d,i} = \omega_i$ ($\omega_{d,i} = \omega_i + \alpha_i$) creates a rotation $X_{\beta_i}^{g \to e}$ ($X_{\beta_i}^{e \to f}$) around the x-axis of the $\{|g\rangle, |e\rangle\}$ ($\{|e\rangle, |f\rangle\}$) Bloch sphere with angle $\int \eta_i(t) dt = \beta_i$ [40, 41]. We set $\lambda_i = 1$ for single qubit operations. A different rotation axis in the equatorial plane can be selected by changing the phase φ_i of the

drive. Similarly, applying a drive on qubit i at the difference frequency between the $|f\rangle$ state of qubit i and the excited resonator state $|1\rangle$, i.e. $\omega_{d,i} = 2\omega_i + \alpha_i - \omega_r$, activates induced Jaynes-Cummings-type vacuum-Rabi oscillations between these states entangling the qubit and the resonator [9]. This can be seen from a perturbation theory argument considering only qubit i, the resonator and the drive, which results in the effective Hamiltonian [9, 42]

$$\hat{H}_{\text{eff},i} = \Delta_{\text{f0}}^{(i)} |f0\rangle\langle f0| + \tilde{g}_i |f0\rangle\langle g1| + \text{h.c.}$$

The qubit state $|e\rangle$ is far detuned and can be ignored. The ac-Stark shift $\Delta_{\text{f0}}^{(i)}$ is to leading order quadratic in the drive strength. The drive frequency can be set to compensate for this ac-Stark shift so that the states $|f0\rangle$ and $|g1\rangle$ form a degenerate subspace allowing for a coherent population transfer between qubit and resonator. The effective coupling strength between $|f0\rangle$ and $|g1\rangle$ is [9]

$$\tilde{g}_i(t) = \frac{g_i \alpha_i \lambda_i \eta_i(t)}{\sqrt{2}\Delta_i(\Delta_i + \alpha_i)}. \tag{2}$$

The rate of the $|f0\rangle \leftrightarrow |g1\rangle$ microwave activated transition decreases with qubit-resonator detuning Δ_i but can be compensated by stronger driving. Rabi rates of 10 MHz have been reported [9]. By contrast, the rate of the cross-resonance gate depends on the qubit-qubit frequency difference. Therefore, an architecture using the holonomy as the two-qubit operation allows a greater qubit-qubit frequency difference and may avoid frequency crowding problems.

Simultaneously applying both drives, illustrated in Fig. 1(b), creates a degenerate subspace spanned by $\{|fg0\rangle, |gf0\rangle, |gg1\rangle\}$. Again, perturbation theory gives the effective Hamiltonian

$$\hat{H}_{\text{eff}}(t) = \Delta_{\text{fg0}} |fg0\rangle\langle fg0| + \Delta_{\text{gf0}} |gf0\rangle\langle gf0| \tag{3}$$
$$+ \tilde{g}_1(t) |fg0\rangle\langle gg1| + \tilde{g}_2(t) |gf0\rangle\langle gg1| + \text{h.c.}$$

with the effective coupling strengths given by Eq. (2). The ac Stark shifts Δ_{fg0} and Δ_{gf0} under this two-tone drive, henceforth named cross ac Stark shifts, may differ in experiment from the ac Stark shifts $\Delta_{\text{f0}}^{(i)}$ under the single tone drive, see Sec. III. The cross ac Stark shifts are removed by appropriately selecting the drive frequencies. To create a holonomic operation and to avoid transitions into dark states [10, 43], the Rabi rates at each point in time must be equal up to the constant scaling parameters λ_i, i.e.

$$\frac{\tilde{g}_1(t)}{\lambda_1} = \frac{\tilde{g}_2(t)}{\lambda_2} = \tilde{g}(t) \; \forall t. \tag{4}$$

Doing so allows us to write the Hamiltonian in Eq. (3) as the product of a time dependent scale factor and a time independent operator

$$\hat{H}'_{\text{eff}}(t) = \tilde{g}(t) \left(\lambda_1 |fg0\rangle\langle gg1| + \lambda_2 |gf0\rangle\langle gg1| + \text{h.c.}\right). \tag{5}$$

Note that Eq. (4) and (2) imply that both pulses have the same envelope $\eta_1(t) = \eta_2(t)$. Under $\hat{H}'_{\text{eff}}$ the system evolves according to

$$|\psi_j(t)\rangle = \exp\left(-i \int_0^t \hat{H}'_{\text{eff}}(\tau)\mathrm{d}\tau\right)|\psi_j(0)\rangle,$$

where $|\psi_j(0)\rangle \in \{|fg0\rangle, |gf0\rangle, |gg1\rangle\}$. States that start in the subspace spanned by $|fg0\rangle$ and $|gf0\rangle$ satisfy the parallel transport condition $\langle\psi_j(t)|\hat{H}'_{\text{eff}}(t)|\psi_k(t)\rangle = 0$, see Appendix A. The evolution is thus purely geometric [10, 43]. If the pulse duration T is chosen such that the evolution is cyclic, i. e. $\int_0^T \tilde{g}_i(t)\mathrm{d}t = \pi$, the final state $|\psi_j(T)\rangle$ returns to its initial subspace $\{|fg0\rangle, |gf0\rangle\}$, see Appendix B. In this basis the resulting operation can be written as the transformation

$$\hat{U} = \begin{pmatrix} \cos\theta & e^{i\phi}\sin\theta \\ e^{-i\phi}\sin\theta & -\cos\theta \end{pmatrix}, \tag{6}$$

where

$$\begin{cases} -e^{i\phi}\tan\dfrac{\theta}{2} = \dfrac{\lambda_1}{\lambda_2}, \\ |\lambda_1|^2 + |\lambda_2|^2 = 1. \end{cases} \tag{7}$$

The form of $\hat{U}$ implies that arbitrary rotations between $|fg\rangle$ and $|gf\rangle$ can be created by changing λ_1 and λ_2. The rotation angle θ controls the amount of population transferred between the qubits. The phase difference between the drives $\phi = \varphi_1 - \varphi_2$ changes the relative phase between $|fg\rangle$ and $|gf\rangle$. The magnitudes of the rotation θ and phase ϕ only depend on λ_i and are controlled at fixed operation time T.

As an example, let $\lambda_1 = \lambda_2 = 1/\sqrt{2}$ and Q1 and Q2 be in the $|f\rangle$ and $|g\rangle$ states, respectively. The drive $\Omega_1(t)$ transfers the population from Q1 to the resonator. Simultaneously, the second drive $\Omega_2(t)$ transfers the population from the resonator to Q2. During this time-evolution the resonator is only partially populated and is completely depleted at the end, as discussed in Sec. V.

III. CALIBRATION OF THE SIMULTANEOUS TWO-TONE DRIVE

To realize the holonomic operation $\hat{U}$ in Eq. (6), the strength, frequency, phase, and duration of each drive must be controlled. In particular, cross ac Stark shifts occurring under simultaneous driving of both qubit-resonator transitions must be compensated to avoid frequency offsets that reduce the fidelity of the population transfer. To keep all ac Stark shifts constant during the holonomic operation, square pulse envelopes are used when driving the $|f0\rangle \leftrightarrow |g1\rangle$ transitions. In short, the calibration is accomplished through the following steps.
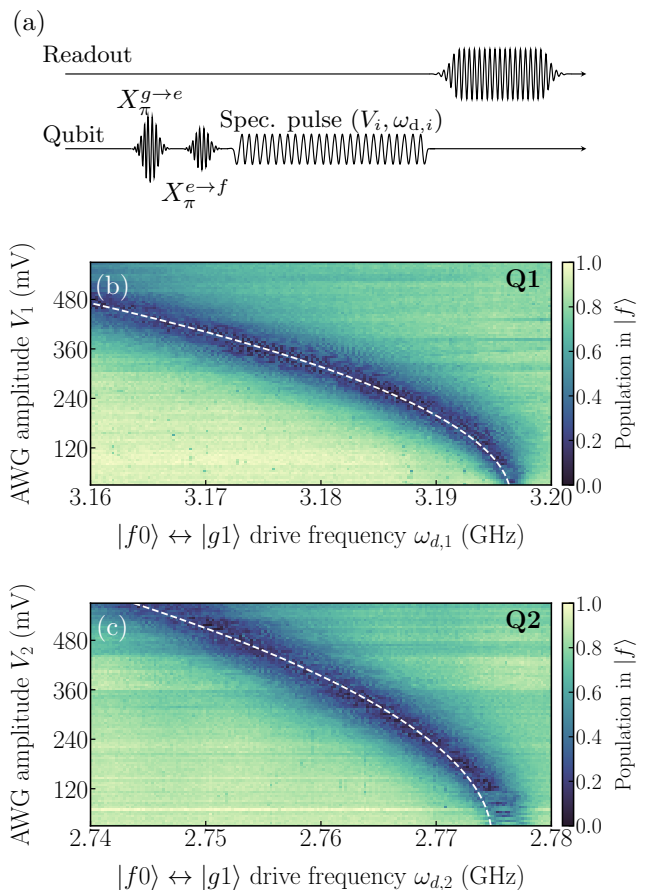

Figure 2. (a) Pulse sequence for qubit and readout tone used to calibrate the ac Stark shifts. (b) and (c) Calibration of the ac Stark shifts for Q1 and Q2 respectively. The qubit $|f\rangle$ population is measured after a spectroscopic square pulse around the targeted $|f0\rangle \leftrightarrow |g1\rangle$ transition. The y-axis is given as voltage amplitude V_i at the output of the arbitrary waveform generator that drives the respective qubit i. For each amplitude the spectrum is fitted to a Lorentzian, see text. The ac-Start shift corrected $|f0\rangle \leftrightarrow |g1\rangle$ frequencies are $\omega^{(i)}_{\text{f0}\leftrightarrow\text{g1}}/(2\pi) = a_i V_1^2 + b_i$ GHz with coefficients $\{a_1, b_1\} = \{-0.164\,\text{GHz/V}^2, 3.196\,\text{GHz}\}$ and $\{a_2, b_2\} = \{-0.094\,\text{GHz/V}^2, 2.775\,\text{GHz}\}$ for Q1 and Q2, respectively.

(i) Measurements of individual ac Stark shifts when applying a single drive $\Omega_i(t)$ result in a calibration curve of frequency shifts as a function of drive amplitude, see Fig. 2.

(ii) Jaynes-Cummings-type oscillations between $|f0\rangle$ and $|g1\rangle$ are measured to calibrate the individual drive amplitudes with $\lambda_i = 1$ such that the induced Rabi rates are equal, i.e. $\tilde{g}_1 = \tilde{g}_2$, see Fig. 3.

(iii) To calibrate cross ac Stark shifts, the population transferred to an initially empty target qubit is measured as a function of drive frequency offset when both drives are applied simultaneously, see

Fig. 4(a).

(iv) Changing the rotation angle θ requires modifying the drive strengths thus producing different (cross) ac Stark shifts. Step (iii) is, therefore, repeated for different θ angles to obtain a θ-dependent calibration curve of cross ac Stark shifts for each drive, see Fig. 4(b).
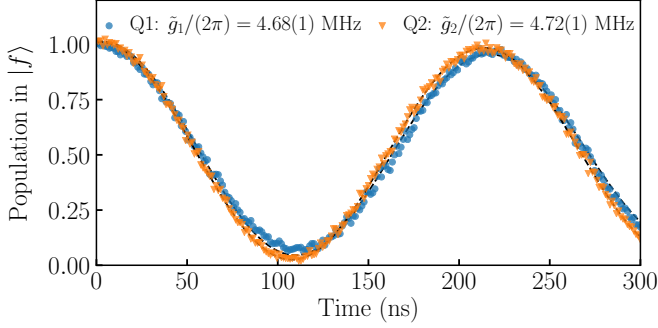

Figure 3. Rabi oscillations between each qubit $|f\rangle$ state and the resonator $|1\rangle$ state. Each qubit is first prepared in $|f\rangle$, then the $|f0\rangle \leftrightarrow |g1\rangle$ drive is applied for a variable time before measuring the qubit. The resulting data set is fitted to a decaying sinusoid to extract the effective coupling strength $\tilde{g}_i$.

In more detail, in step (i) the ac Stark shift induced by the $|f0\rangle \leftrightarrow |g1\rangle$ drive of each qubit is determined for a range of drive amplitudes. Spectroscopy on the $|f0\rangle \leftrightarrow |g1\rangle$ transition of each qubit yields the $\Delta_{\mathrm{f0}}^{(i)}(\Omega_i)$ ac Stark shift calibration curve. In each data set the relevant qubit is prepared in the $|f\rangle$ state by applying a $X_\pi^{g \to e}$ π-pulse followed by a $X_\pi^{e \to f}$ π-pulses. Next, a $10\ \mu s$ spectroscopic pulse is applied at a fixed amplitude and frequency and the qubit is measured, see Fig. 2(a). This pulse sequence is repeated for different amplitudes and frequencies. The resonance line is fitted to a second-order polynomial in drive amplitude shown by the white dashed line in Fig. 2(b)-(c). In the limit of zero drive amplitude the frequencies of the $|f0\rangle \leftrightarrow |g1\rangle$ drives are 3.196 GHz and 2.775 GHz for Q1 and Q2, respectively. Henceforth, all frequency shifts in the following figures will be referenced to these values.

In the next step (ii), the amplitude of each drive (applied separately) is adjusted to produce rotations between the qubit $|f\rangle$ and the resonator $|1\rangle$ state at equal Rabi rates. With a target duration of $T = 213$ ns we obtain $\tilde{g}_1/(2\pi) = 4.69(1)$ MHz and $\tilde{g}_2/(2\pi) = 4.72(1)$ MHz for Q1 and Q2, respectively, see Fig. 3. For this, the calibration of the ac Stark shifts of step (i) is used to adjust the drive frequency.
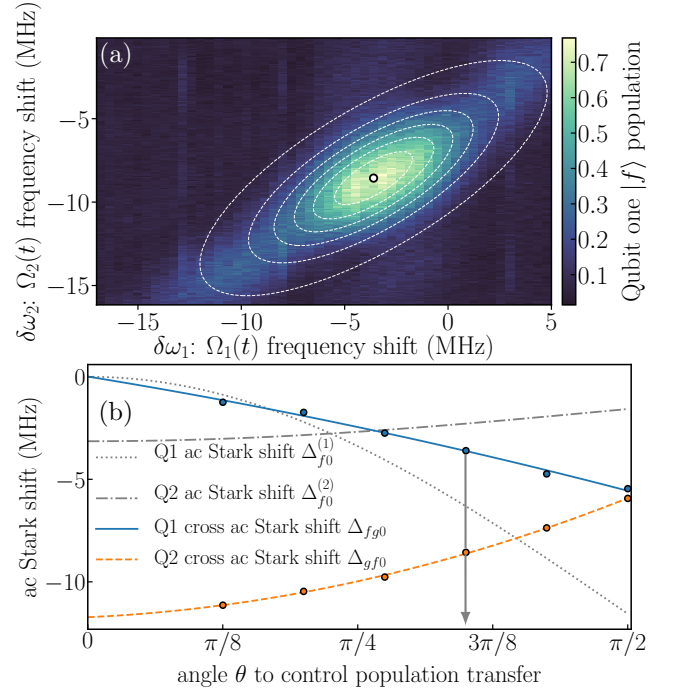

Figure 4. (a) Population transferred to Q1 as function of the frequency shifts applied to both drives when $\theta = 1.1$ rad and Q2 is initially in state $|f\rangle$. The dashed lines show a Gaussian fit to determine the frequency shifts $\delta\omega_1$ and $\delta\omega_2$ for optimal population transfer indicated by the dot. (b) Measured values (points) and calibration curves (lines) for the compensation of the θ-dependent cross ac Stark shifts during two-tone driving. The optimal value for $\theta = 1.1$ rad in (a) is indicated by an arrow. The ac Stark shifts $\Delta_{f0}^{(i)}$ are the fitted curves from Fig. 2. In both (a) and (b) frequency shifts are relative to the zero-amplitude offsets 3.196 GHz and 2.775 GHz for Q1 and Q2, respectively.

In step (iii) both drives are simultaneously applied for a duration T. To quantify the cross ac Stark shifts the frequencies of both drives are varied by offsets $\delta\omega_i$ and the population transfer between the qubits is measured. For this, Q2 is prepared in state $|f\rangle$, then both drives are applied, finally the population in Q1 is measured. The population is fitted to a 2D Gaussian function to obtain the frequency offsets $(\Delta_{fg0}, \Delta_{gf0})$ that are equal to the $\delta\omega_i$ values of maximum population transfer and therefore compensate the cross ac Stark shifts, see Fig. 4(a).

The measured cross ac Stark shifts differ from the ac Stark shifts $\Delta_{\mathrm{f0}}^{(i)}$ obtained when a single tone is applied, see Fig. 4(b). This effect is not observed in the simulations discussed in Sec. V. We therefore attribute the extra shifts to drive-induced crosstalk and/or unwanted qubit-qubit interactions resulting from static capacitive coupling. In the last step (iv) we determine the dependence of the cross ac Stark shifts on the θ angles, which is adjusted by the drive amplitude ratio λ_1/λ_2. For this, step (iii) is repeated for different θ. The cross ac Stark shifts $(\Delta_{fg0}(\theta), \Delta_{gf0}(\theta))$ are fitted to a second-order function

in θ yielding a calibration curve for each drive, see Fig. 4(b).

The cross ac Stark shifts acting on the qubits during the simultaneous driving leads to an additional phase shift of the individual qubit states. This induces a systematic θ-dependent phase shift on the qubit states that is removed a posteriori in the data so as not to affect fidelity measurements. Alternatively, such phase shifts can also be removed in software [44].

IV. PREPARATION OF ENTANGLED STATES

To form entangled states as arbitrary superpositions of $|eg\rangle$ and $|ge\rangle$, one qubit (source) is prepared in state $|f\rangle$, the two-tone holonomic operation coherently transfers some population to the $|f\rangle$ state of the other qubit (target), and a final $X_\pi^{f\to e}$ pulse maps the qubit $|f\rangle$ populations back to $|e\rangle$. With the chosen rate of $\tilde{g}/(2\pi) = 4.70$ MHz for the holonomic operation and $\theta = \pi/4$, a fully-entangled Bell state $|\Psi\rangle = (|eg\rangle + e^{i\varphi}|ge\rangle)/\sqrt{2}$, is formed by a pulse of duration 213 ns. A state fidelity $\mathcal{F} = \text{Tr}\{\sqrt{\sqrt{\rho_T}\rho_M\sqrt{\rho_T}}\} = 95.2\%$ (95.3%) is obtained for Q1 (Q2) as the source qubit with the ideal target state density matrix $\rho_T = |\Psi\rangle\langle\Psi|$ and the measured density matrix ρ_M. ρ_M is determined using state tomography with 1000 repeated single-shot measurements, see Fig. 5.
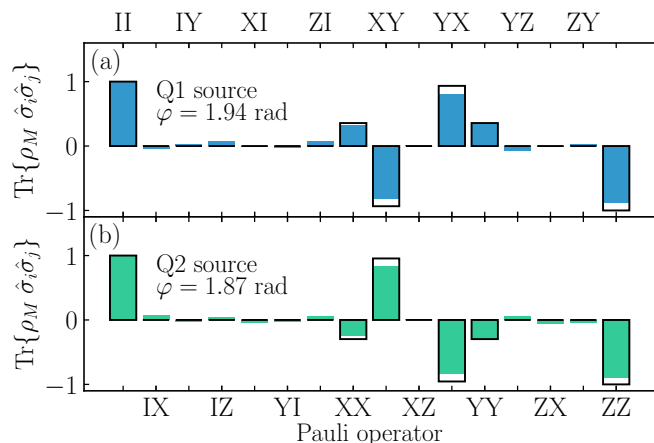

Figure 5. Pauli-operator representation of the entangled state $|\Psi\rangle = (|eg\rangle + e^{i\varphi}|ge\rangle)/\sqrt{2}$ with 95.3% and 95.2% fidelity when the source qubit is Q1 (a) and Q2 (b), respectively. The solid black lines show the ideal values.

To demonstrate control over the angles θ and ϕ, quantum state tomography has been done on 900 states generated with 30 different linearly spaced values of $\theta \in [0, \pi/2]$ and $\phi \in [0, 2\pi]$. For each state the fidelity $\mathcal{F}$ has been measured with Q1 used as the source qubit. Scaling the drives by λ_1 and λ_2 according to Eq. (7) produces the different θ-angles transferring $\sin(\theta)^2$ of population from

the source qubit to the target qubit. Changing the phase ϕ_2 of the drive on Q2 changes the measured angle φ.

For each value of θ, the populations in the source qubit and target qubit, extracted from the density matrix, are averaged over the different phase values ϕ. As θ increases, more population is transferred to the target qubit in good agreement with theory, see Fig. 6(a). The state fidelities averaged over ϕ are lower for larger θ, see Fig. 6(b). We attribute this to the large charge dispersion (determined by Ramsey-type measurements) of 1.8 MHz and 3.0 MHz on the $|f\rangle$ states of Q1 and Q2 respectively, as confirmed by numerical simulations discussed in Sec. V.
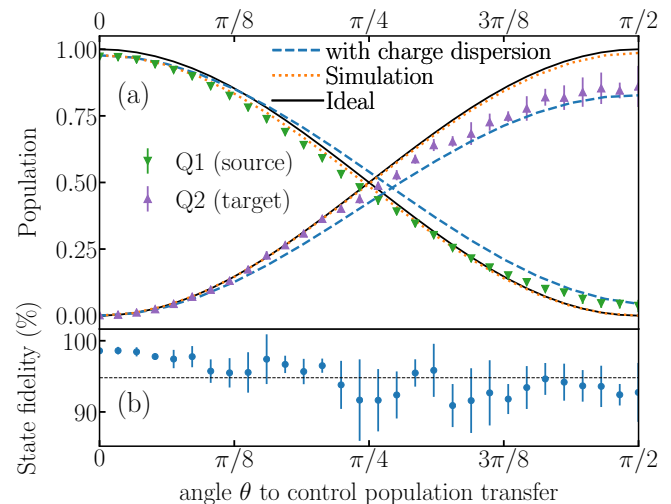

Figure 6. State transfer from Q1 to Q2 as a function of the angle θ. (a) Population in the source (Q1) and target qubit (Q2) extracted from quantum state tomography in the qubit $\{|e\rangle, |g\rangle\}$ subspace. The solid lines indicate ideal values. The dotted lines are a simulation showing the effect of T_1 on the ideal population transfer. The dashed lines show a simulation of the effect of charge dispersion and T_1. (b) State fidelity after transferring an amount of population controlled by θ. Each point is the state fidelity average over 30 different values of ϕ. The average state fidelity is 94.8%.

Control over ϕ is demonstrated using the density matrices with $\theta \in [0.19\pi, 0.31\pi]$ from which the phase between $|eg\rangle$ and $|ge\rangle$ can be measured and compared to the expected phase, see Fig. 7. This θ-range is used since the measured phase between $|eg\rangle$ and $|ge\rangle$ is more accurate when both states have large populations. In 8.3% of the measurements, a large systematic phase error of 834 ± 81 mrad was observed, which we attribute to charge noise. These data points are not shown in the figure. The difference between the expected and measured relative phase φ between the $|eg\rangle$ and $|ge\rangle$ states for $\varphi \neq 0$ is -2 ± 42 mrad, see Fig. 7(b). The small mean shows that ϕ can be set with high accuracy. The large standard deviation reflects measurement imperfections of the density matrix and includes the measured timing jitter $\sigma_{\text{jitter}} = 2.6$ ps between

the two drives. This corresponds to a 7 mrad imprecision in φ computed from $2\pi\sigma_{\text{jitter}}(3.196 \text{ GHz} - 2.775 \text{ GHz})$.
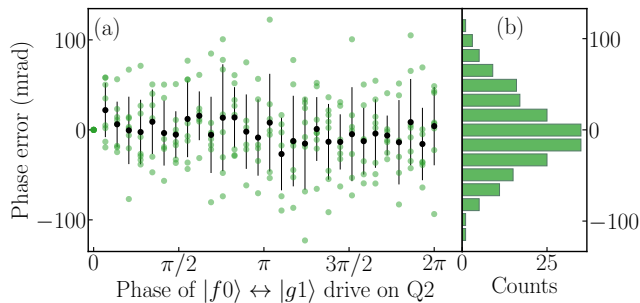

Figure 7. (a) Difference between expected and measured phases (between $|ge\rangle$ and $|eg\rangle$) obtained from quantum state tomography as a function of the phase of the drive applied to Q2. Each green point corresponds to different value of θ and ϕ. The black dots show the average over θ. The data points at the set phase $\phi = 0$ are used to remove the systematic single-qubit phases induced by θ-dependent cross ac Stark shifts leading to zero dispersion of the first point. (b) Histogram of the errors, the mean and standard deviation of all points are -2 mrad and 42 mrad, respectively.

V. SIMULATION RESULTS

The holonomic operation is simulated using QuTiP [45] to understand leading error contributions. We use the Hamiltonian in Eq. (1) with the qubits modeled as anharmonic four-level systems and the resonator modeled as a harmonic three-level system. Experimentally determined frequencies, anharmonicities, coupling strengths and T_1 times are taken into account when computing the time evolution using a master equation in Lindblad form. As in the experiment, we assume that one of the qubits starts in the $|f\rangle$ state. The control pulse is a flat-top Gaussian with 206 ns long top and $\sigma = 3.5$ ns to reflect the effect of the finite bandwidth of the experimental setup on the square pulse.

The simulated time evolution of a population transfer from Q1 to Q2 shows that the resonator is populated during the holonomic operation and returns to its initial ground state at the end of the pulse, see Fig. 8(a) for an example with $\theta = \pi/2$. Here the maximum population reached in the resonator is 50%. Table I summarizes simulation results of end populations for different T_1 times of the qubits and the resonator. For unitary dynamics ($T_1 \to \infty$), the target state is reached with 99.98% fidelity. If relaxation processes for both qubits and resonator are included, this value decreases to 98.48%, with some residual population in the $|e\rangle$ states due to the finite T_1 time of the qubits. The short T_1 time of the resonator only marginally decreases the amount of population transferred, as can be seen from the fidelity of 99.11% reached when assuming no relaxation in

the resonator but finite T_1 times of the qubits. However, the effect of the 1.8 MHz and 3.0 MHz charge dispersion on Q1 and Q2, respectively, is detrimental. We simulate this effect by imposing a frequency shift $-0.9 \text{ MHz} \leq \delta\omega_1/(2\pi) \leq 0.9 \text{ MHz}$ on the drive of Q1 and $-1.5 \text{ MHz} \leq \delta\omega_2/(2\pi) \leq 1.5 \text{ MHz}$ on the drive of Q2. For each pair of frequency shifts on this two-dimensional grid we compute the time dynamics for different θ-angles. We average the final population in each qubit over the two-dimensional grid assuming that the offset charge n_{g} due to the electrostatic environment has a uniform probability distribution. Since the qubit frequency is a sinusoid function in n_{g} [46] the probability distribution function for $\delta\omega_i$ is $f_i(\delta\omega_i) = 1/(\pi\sqrt{\delta\omega_{i,\text{max}}^2 - \delta\omega_i^2})$ where $\delta\omega_{i,\text{max}}/(2\pi)$ is 0.9 MHz and 1.5 MHz for Q1 and Q2, respectively. The population transfer with the simulated charge noise matches well the experimental data, see Fig. 6(a). As seen from the last entry in Tab. I, with such large charge dispersion the population is not properly transferred between the qubits and partially remains in the resonator, see Fig. 8(b) for an example in which $(\delta\omega_1/(2\pi), \delta\omega_2/(2\pi)) = (0.9, 0)$ MHz and $\theta = \pi/2$. We expect that by slightly modifying the charging energies of the transmons, charge noise can be significantly suppressed: for example requiring less than 10 kHz charge dispersion in the $|f\rangle$ state can be achieved with an $E_C \leq 217$ MHz for a 5.0 GHz qubit [4].
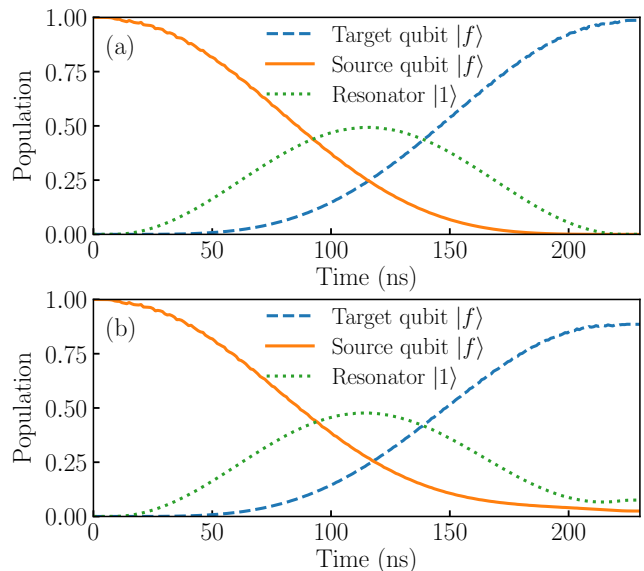

Figure 8. Simulation of the time evolution when $\theta = \pi/2$ and Q1 is the source qubit. (a) Time evolution assuming the drives are calibrated using the procedure in Sec. III. (b) Simulated time evolution when the drive on Q1 is 0.9 MHz detuned.

Table I. Final populations in the different states of the system rounded to 10^{-4} after a flat-top Gaussian pulse with 206 ns long top and $\sigma = 3.5$ ns that swaps the population from $|fg0\rangle$ into $|gf0\rangle$. The numbers are expressed as a percentage.

Unitary time evolution					
$|gf0\rangle$	$|gg0\rangle$	$|eg0\rangle$	$|ge0\rangle$	$|gg1\rangle$	$|fg0\rangle$
99.98	0	0	0	0.02	0
Finite T_1					
$|gf0\rangle$	$|gg0\rangle$	$|eg0\rangle$	$|ge0\rangle$	$|gg1\rangle$	$|fg0\rangle$
98.62	0.87	0.19	0.29	0.02	0
Finite qubit T_1, Resonator $T_1 \rightarrow \infty$					
$|gf0\rangle$	$|gg0\rangle$	$|eg0\rangle$	$|ge0\rangle$	$|gg1\rangle$	$|fg0\rangle$
99.11	0.01	0.37	0.5	0.02	0
Finite T_1 with charge dispersion					
$|gf0\rangle$	$|gg0\rangle$	$|eg0\rangle$	$|ge0\rangle$	$|gg1\rangle$	$|fg0\rangle$
82.73	0.98	0.17	0.3	11.38	4.44

VI. QUANTUM CHEMISTRY

The two-tone holonomic operation conserves the excitation number, see Eq. (6). This property makes it well suited for quantum chemistry applications where the number of electrons is fixed [39]. As an example, we use the holonomy to compute the ground state of molecular hydrogen, a system that has been used as an experimental benchmark for performing quantum chemsitry calculations in various platforms [47–53]. This fermionic problem, in a minimal STO-3G basis, is first mapped to the qubit Hamiltonian

$$\hat{H}_{H_2} = \alpha_1 II + \alpha_2 \hat{I} \hat{\sigma}_2^{(z)} + \alpha_3 \hat{\sigma}_1^{(z)} \hat{I} \qquad (8)$$
$$+ \alpha_4 \hat{\sigma}_1^{(x)} \sigma_2^{(x)} + \alpha_5 \hat{\sigma}_1^{(y)} \sigma_2^{(y)} + \alpha_6 \hat{\sigma}_1^{(z)} \sigma_2^{(z)},$$

where the overlap integrals α_i depend on the bond length d [47] and $\hat{\sigma}_i^{(j)}$ are qubit Pauli operators. Equation (8) describes the two-electron subspace of the H_2 molecule restricted to states with zero magnetic moment. In this model, the energy of the ground state E_0 is found by minimizing the expectation value of $\hat{H}_{H_2}$ for trial states $|\psi(\theta, \phi)\rangle \in \{|ge\rangle, |eg\rangle\}$.

To create the trial states we apply a first $X_\pi^{g \rightarrow e}$ pulse followed by a $X_\pi^{e \rightarrow f}$ pulse to Q1. We then use the two-tone holonomic drive to create the state $\cos\theta |fg\rangle + e^{i\phi} \sin\theta |gf\rangle$. The angles θ and ϕ are controlled by $\lambda_{1,2}$, see Eq. (7). A final $X_\pi^{f \rightarrow e}$ pulse applied to each qubit maps the population in the $|f\rangle$ states back to the $|e\rangle$ states. The resulting trial state $|\psi(\theta, \phi)\rangle = \cos\theta |eg\rangle + e^{i\phi} \sin\theta |ge\rangle$ is used to measure the expectation value of the correlators in Eq. (8).

In a scalable calculation of molecular energies using a quantum computer, the energies would be found with a search algorithm using the variational quantum eigensolver method (VQE) [47, 49, 54, 55]. However, the parameter space of the H_2 molecule is small enough such that this can be done with a two-dimensional scan over θ and ϕ. We calculate the energy of the molecule for θ and
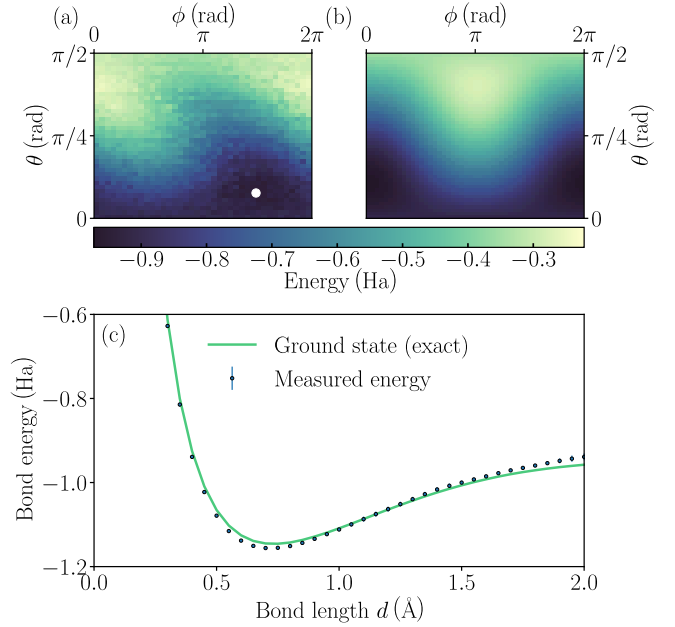

Figure 9. Measurement of the ground state energy of the H_2 molecule using the two-tone holonomic operation. (a) energy of H_2 as function of θ and ϕ for a $d = 1.4$ Å bond length. Each point is obtained by measuring the correlators in Eq. (8) and weighing them by the overlap integrals $\alpha_i(d)$. Each data point corresponds to the average of three measurements with 1000 shots each. The white dot in (a) indicates the minimum measured energy. (b) Theoretical calculation of the ground state energy of H_2 obtained by diagonalizing $\hat{H}_{H_2}$ for a $d = 1.4$ Å bond length. (c) Dissociation curve of molecular hydrogen obtained by computing E_0 for different bond lengths using the measured correlators that make up the energy map shown in (a).

ϕ values ranging between $[0, \pi/2]$ and $[0, 2\pi]$, respectively, which results in an energy map $E(\theta, \phi)$, see Fig. 9(a) for an example with bond length $d = 1.4$ Å. The ground state energy is given by the point with the lowest energy, as indicated by the white dot in Fig. 9(a). Comparing the measured data in Fig. 9(a) to the theoretical energy map, shown in Fig. 9(b), reveals a θ-dependent phase offset which twists the (θ, ϕ) energy map. We believe that this error is induced by ac Stark shifts. Despite this effect, we still manage to find the ground state energy. This observation provides support to the hypothesis that variational quantum chemistry is robust to some unitary errors [49]. Identifying the minimum energy for different bond lengths yields the dissociation curve of molecular hydrogen shown in Fig. 9(c). We observe a deviation with respect to the theoretical curve which increases with bond length. In our model the ground state energy for longer bond lengths d is obtained at larger θ-values. We therefore attribute the deviation with theory mainly to charge noise, see Fig. 6(b). For bond lengths below 1.85 Å the α_3 factor that multiplies the $\langle I \hat{\sigma}_2^{(z)} \rangle$ correlator is negative. Errors that reduce the magnitude of all

other correlators with respect to $\langle I\hat{\sigma}_2^{(z)}\rangle$ may thus result in data points lying below the theoretical curve.

VII. CONCLUSION AND OUTLOOK

We have demonstrated entanglement creation and manipulation of two-qubit states using non-adiabatic holonomic operations. Using square pulses lasting 213 ns we have created two-qubit states with fidelities above 95%. This fidelity is also affected by imperfections of the single qubit rotations $X_\alpha^{i\to j}$ with gate fidelities of 98% as determined by quantum process tomography. Simulations have identified charge dispersion in the qubit $|f\rangle$ states as the main fidelity limitation. With reduced charge dispersion, population transfers with higher fidelity are possible. Further gains in fidelity can be obtained by increasing the T_1 time of the resonator, e.g. by optimizing its geometry [56]. In the future, the holonomic operation presented here may be extended to a two-qubit non-Abelian non-adiabatic gate [57]. For this to be possible, the 1-2 excitation manifold $\{|gg1\rangle, |fg0\rangle, |gf0\rangle\}$ must be well separated from the transitions in the 3-4 excitation manifold $\{|fg1\rangle, |gf1\rangle, |ff0\rangle\}$ to avoid residual driving of these transitions. In our sample, the separation between these manifolds was 5 MHz. A larger separation will permit the operation described in Eq. (6) as a SWAP-type gate that acts on the full computational subspace without population loss. A larger separation can be achieved by increasing the dispersive shift between the coupling resonator and the qubits. Alternatively, it may be possible to use more complex pulse shapes obtained by optimal control methods [58, 59] applied to superconducting qubits [60, 61].

From a practical perspective the holonomic operation provides a potential solution to the frequency-crowding issue when using cross-resonance gates in all-microwave architectures: a greater qubit-resonator frequency difference can be compensated by a stronger drive whereas in the case of the cross-resonance gate the qubit-qubit frequency difference has to be similar to the qubit anhrmonicity. A second important aspect is that the holonomy provides an excitation preserving interaction that restricts the dimension of the state space explored in VQE-based quantum chemsitry calculations. It can, thus, lead to a faster convergence with algorithms that have shorter circuit-depth [39].

VIII. ACKNOWLEDGMENTS

Appendix A: Dynamics

Here we show that the evolution in the two-qubit subspace governed by the Hamiltonian $\hat{H}'_{\text{eff}}$ from Eq. (5) is purely geometric by following a parallel transport. Consider two orthonormal vectors that initially span the qubit subspace $\{|fg0\rangle, |gf0\rangle\}$

$$|\psi_1(0)\rangle = \alpha|fg0\rangle + \beta|gf0\rangle$$
$$|\psi_2(0)\rangle = \beta^*|fg0\rangle - \alpha^*|gf0\rangle,$$

where $\alpha, \beta \in \mathbb{C}$ and $|\alpha|^2 + |\beta|^2 = 1$. We define the initial subspace $S_0 = \text{span}\{|\psi_1(0)\rangle, |\psi_2(0)\rangle\}$. Under the action of $\hat{H}'_{\text{eff}}$ this subspace evolves into $S_t = \text{span}\{|\psi_1(t)\rangle, |\psi_2(t)\rangle\}$. The time evolution satisfies the parallel transport condition

$$\langle\psi_j(t)|\hat{H}'_{\text{eff}}(t)|\psi_k(t)\rangle = 0 \qquad (A1)$$

which can be transformed into $\langle\psi_j(t)|\dot{\psi}_k(t)\rangle = 0$ using the Schrodinger equation. This implies that an infinitesimally small time-step dt evolves the vector $|\psi_k(t)\rangle$ along a direction which is perpendicular to all vectors in S_t, i. e. there are no transitions between the vectors in S_t during the time evolution. This means that the resulting non-Abelian geometric phase has no dynamical contributions [21].

Now we show that Eq. (A1) holds when the Hamiltonian $\hat{H}'_{\text{eff}}$ is given by Eq. (5). We write $\hat{H}'_{\text{eff}}(t) = \tilde{g}(t)\hat{A}$, where

$$\hat{A} = \begin{pmatrix} 0 & \lambda_1 & 0 \\ \lambda_1^* & 0 & \lambda_2 \\ 0 & \lambda_2^* & 0 \end{pmatrix}$$

in the basis $|fg0\rangle = (1,0,0)^T$, $|gg1\rangle = (0,1,0)^T$ and $|gf0\rangle = (0,0,1)^T$. The time evolution operator is

$$\hat{U}(t) = \mathcal{T}\exp\left(-i\int_0^t \tilde{g}(t')\hat{A}dt\right) = \exp\left(-iG(t)\hat{A}\right)$$

where $G = \int_0^t \tilde{g}(t')dt'$ and $\mathcal{T}$ denotes time-ordering. The last equation follows from the time-independence of $\hat{A}$ resulting in $\hat{H}'_{\text{eff}}$ commuting with itself at all times. The left-hand side of Eq. (A1) can be written as $\tilde{g}(t)\langle\psi_j(0)|\hat{U}(t)^\dagger\hat{A}\hat{U}(t)|\psi_k(0)\rangle$. Since $[\hat{U}, \hat{A}] = 0$ the term $\hat{U}^\dagger\hat{A}\hat{U}$ reduces to $\hat{A}$. The action of $\hat{A}$ on $|\psi_1(0)\rangle$ and $|\psi_2(0)\rangle$ yields a vector proportional to $|gg1\rangle$ which is perpendicular to $|\psi_j(0)\rangle$ for $j = 1, 2$. The parallel transport condition is thus satisfied $\forall$ t.

Appendix B: Cyclical evolution

Since $|\lambda_1|^2 + |\lambda_2|^2 = 1$, $\hat{A}$ satisfies $\hat{A}^3 = \hat{A}$ resulting in $\hat{A}^{2n+1} = \hat{A}$ and $\hat{A}^{2n} = \hat{A}^2$ for $n \geq 1$ where

$$\hat{A}^2 = \begin{pmatrix} |\lambda_1|^2 & 0 & \lambda_1\lambda_2 \\ 0 & 1 & 0 \\ \lambda_1^*\lambda_2^* & 0 & |\lambda_2|^2 \end{pmatrix}.$$

Using the Taylor expansion for the exponential, cosine and sine functions the time evolution operator is

$$\hat{U}(t) = I + \hat{A}^2\{\cos[G(t)] - 1\} - i\hat{A}\sin[G(t)].$$

When $G(T) = \pi$ the time evolution operator reads $\hat{U}(\tau) = I - 2\hat{A}^2$. The evolution is thus cyclical, i. e. $S_T = S_0$, since $\hat{A}^2$ does not mix the subspace $\{|fg0\rangle, |gf0\rangle\}$ and $\{|gg1\rangle\}$. By introducing $-e^{i\phi}\tan(\theta/2) = \lambda_1/\lambda_2$ one recovers the time evolution operator of Eq. (6) in the main text.

[1] Michel H. Devoret and Robert J. Schoelkopf, "Superconducting circuits for quantum information: An outlook," Science **339**, 1169–1174 (2013).

[2] William D. Oliver and Paul B. Welander, "Materials in superconducting quantum bits," MRS Bulletin **38**, 816–825 (2013).

[3] J. B. Chang, M. R. Vissers, A. D. Corcoles, M. Sandberg, J. Gao, D. W. Abraham, J. M. Chow, J. M. Gambetta, M. B. Rothwell, G. A. Keefe, M. Steffen, and D. P. Pappas, "Improved superconducting qubit coherence using titanium nitride," Appl. Phys. Lett. **103**, 012602 (2013).

[4] J. Koch, T. M. Yu, J. Gambetta, A. A. Houck, D. I. Schuster, J. Majer, A. Blais, M. H. Devoret, S. M. Girvin, and R. J. Schoelkopf, "Charge-insensitive qubit design derived from the Cooper pair box," Phys. Rev. A **76**, 042319 (2007).

[5] Alexandre Blais, Jay Gambetta, Andreas Wallraff, David I. Schuster, Steven M. Girvin, Michel H. Devoret, and Robert J. Schoelkopf, "Quantum-information processing with circuit quantum electrodynamics," Phys. Rev. A **75**, 032329–21 (2007).

[6] J. Majer, J. M. Chow, J. M. Gambetta, J. Koch, B. R. Johnson, J. A. Schreier, L. Frunzio, D. I. Schuster, A. A. Houck, A. Wallraff, A. Blais, M. H. Devoret, S. M. Girvin, and R. J. Schoelkopf, "Coupling superconducting qubits via a cavity bus," Nature **449**, 443–447 (2007).

[7] Chad Rigetti and Michel Devoret, "Fully microwave-tunable universal gates in superconducting qubits with linear couplings and fixed transition frequencies," Phys. Rev. B **81**, 134507 (2010).

[8] Sarah Sheldon, Easwar Magesan, Jerry M. Chow, and Jay M. Gambetta, "Procedure for systematically tuning up cross-talk in the cross-resonance gate," Phys. Rev. A **93**, 060302 (2016).

[9] Sina Zeytinoglu, Marek Pechal, Simon Berger, Abdufarrukh A. Abdumalikov, Andreas Wallraff, and Stefan Filipp, "Microwave-induced amplitude- and phase-tunable qubit-resonator coupling in circuit quantum electrodynamics," Phys. Rev. A **91**, 043846 (2015).

[10] Erik Sjöqvist, D. M. Tong, Mauritz L. Andersson, Björn Hessmo, Markus Johansson, and Kuldip Singh, "Nonadiabatic holonomic quantum computation," New J. Phys. **14**, 103035 (2012).

[11] Abdufarrukh A. Abdumalikov, Johannes M. Fink, Kristinn Juliusson, Marek Pechal, Simon Berger, Andreas Wallraff, and Stefan Filipp, "Experimental realization of non-abelian non-adiabatic geometric gates," Nature **496**, 482 (2013).

[12] Silvia Arroyo-Camejo, Andrii Lazariev, Stefan W. Hell, and Gopalakrishnan Balasubramanian, "Room temperature high-fidelity holonomic single-qubit gate on a solid-state spin," Nat. Commun. **5**, 4870 (2014).

[13] Simone Gasparinetti, Simon Berger, Abdufarrukh A. Abdumalikov Jr., Marek. Pechal, Stefan Filipp, and Andreas Wallraff, "Measurement of a vacuum-induced geometric phase," Sci. Adv. **2** (2016).

[14] Hang Li, Yang Liu, and Gui Lu Long, "Experimental realization of single-shot nonadiabatic holonomic gates in nuclear spins," Sci. China Phys. Mech. **60**, 080311 (2017).

[15] Yuhei Sekiguchi, Naeko Niikura, Ryota Kuroiwa, Hiroki Kano, and Hideo Kosaka, "Optical holonomic single quantum gates with a geometric spin under a zero field," Nat. Photon. **11**, 309–314 (2017).

[16] Brian B. Zhou, Paul C. Jerger, Vladislav O. Shkolnikov, F. Joseph Heremans, Guido Burkard, and David D. Awschalom, "Holonomic quantum control by coherent optical excitation in diamond," Phys. Rev. Lett. **119**, 140503 (2017).

[17] Sergey Danilin, Antti Vepsäläinen, and Gheorghe S. Paraoanu, "Experimental state control by fast non-abelian holonomic gates with a superconducting qutrit," Physica Scripta **93**, 055101 (2018).

[18] Naoki Ishida, Takaaki Nakamura, Touta Tanaka, Shota Mishima, Hiroki Kano, Ryota Kuroiwa, Yuhei Sekiguchi, and Hideo Kosaka, "Universal holonomic single quantum gates over a geometric spin with phase-modulated polarized light," Opt. Lett. **43**, 2380–2383 (2018).

[19] Y. Xu, W. Cai, Y. Ma, X. Mu, L. Hu, Tao Chen, H. Wang, Y. P. Song, Zheng-Yuan Xue, Zhang-qi Yin, and L. Sun, "Single-loop realization of arbitrary nonadiabatic holonomic single-qubit quantum gates in a superconducting circuit," Phys. Rev. Lett. **121**, 110501 (2018).

[20] Paolo Zanardi and Mario Rasetti, "Holonomic quantum computation," Phys. Lett. A **264**, 94 – 99 (1999).

[21] Erik Sjoqvist, "Geometric phases in quantum information," Int. J. Quantum Chem. **115**, 1311–1326 (2015).

[22] Alexandre Blais and André-Marie S. Tremblay, "Effect of noise on geometric logic gates for quantum computation," Phys. Rev. A **67**, 012308 (2003).

[23] Robert S. Whitney and Yuval Gefen, "Berry phase in a nonisolated system," Phys. Rev. Lett. **90**, 190402 (2003).

[24] Gabriele De Chiara and Gioacchino Massimo Palma, "Berry phase for a spin 1/2 particle in a classical fluctuating field," Phys. Rev. Lett. **91**, 090404 (2003).

[25] Angelo Carollo, Ivette Fuentes-Guridi, Marcelo F. Santos, and Vlatko Vedral, "Geometric phase in open systems," Phys. Rev. Lett. **90**, 160402 (2003).

[26] Paolo Solinas, Paolo Zanardi, and Nino Zanghì, "Robustness of non-abelian holonomic quantum gates against parametric noise," Phys. Rev. A **70**, 042316 (2004).

[27] P. J. Leek, J. M. Fink, A. Blais, R. Bianchetti, M. Göppl, J. M. Gambetta, D. I. Schuster, L. Frunzio, R. J. Schoelkopf, and A. Wallraff, "Observation of Berry's phase in a solid-state qubit," Science **318**, 1889 (2007).

[28] Stefan Filipp, Juergen Klepp, Yuji Hasegawa, Christian Plonka-Spehr, Ute Schmidt, Peter Geltenbort, and Helmut Rauch, "Experimental demonstration of the stability of Berry's phase for a spin-1/2 particle," Phys. Rev. Lett. **102**, 030404 (2009).

[29] Fernando M. Cucchietti, Jingfu Zhang, Fernando C. Lombardo, Paula I. Villar, and Raymond Laflamme, "Geometric phase with nonunitary evolution in the presence of a quantum critical bath," Phys. Rev. Lett. **105**, 240406 (2010).

[30] Simon Berger, Marek Pechal, Abdufarrukh A. Abdumalikov Jr., Christopher Eichler, Lars Steffen, Alexey Fedorov, Andreas Wallraff, and Stefan Filipp, "Exploring the effect of noise on the Berry phase," Phys. Rev. A **87**, 060303(R) (2013).

[31] H. Wu, E. M. Gauger, R. E. George, M. Möttöonen, H. Riemann, N. V. Abrosimov, P. Becker, H.-J. Pohl, K. M. Itoh, M. L. W. Thewalt, and J. J. L. Morton, "Geometric phase gates with adiabatic control in electron spin resonance," Phys. Rev. A **87**, 032326 (2013).

[32] Simon Berger, Marek Pechal, Philipp Kurpiers, Abdufarrukh A. Abdumalikov, Christopher Eichler, Jonas A. Mlynek, Alexander Shnirman, Yuval Gefen, Andreas Wallraff, and Stefan Filipp, "Measurement of geometric dephasing using a superconducting qubit," Nat. Commun. **6**, 8757 (2015).

[33] Shi-Biao Zheng, Chui-Ping Yang, and Franco Nori, "Comparison of the sensitivity to systematic errors between nonadiabatic non-abelian geometric gates and their dynamical counterparts," Phys. Rev. A **93**, 032313 (2016).

[34] Markus Johansson, Erik Sjöqvist, Mauritz L. Andersson, Marie Ericsson, Björn Hessmo, Kuldip Singh, and D. M. Tong, "Robustness of non-adiabatic holonomic gates," Phys. Rev. A **86**, 062322 (2012).

[35] Ingo Kamleitner, Paolo Solinas, Clemens Müller, Alexander Shnirman, and Mikko Möttönen, "Geometric quantum gates with superconducting qubits," Phys. Rev. B **83**, 214518 (2011).

[36] Chong Zu, W.-B. Wang, Li He, W.-G. Zhang, Chengyu Dai, Fei Wang, and Luming Duan, "Experimental realization of universal geometric quantum gates with solid-state spins," Nature **514**, 72–75 (2014).

[37] Guanru Feng, Guofu Xu, and Gui Lu Long, "Experimental realization of nonadiabatic holonomic quantum computation," Phys. Rev. Lett. **110**, 190501 (2013).

[38] International Business Machines Corporation, "IBM Q Experience," (2016).

[39] P. Kl. Barkoutsos, J. F. Gonthier, I. Sokolov, N. Moll, G. Salis, A. Fuhrer, M. Ganzhorn, D. J. Egger, M. Troyer, A. Mezzacapo, S. Filipp, and I. Tavernelli, "Quantum algorithms for electronic structure calculations: Particle-hole hamiltonian and optimized wave-function expansions," Phys. Rev. A **98**, 022322 (2018).

[40] Felix Motzoi, Jay M. Gambetta, Patrick Rebentrost, and Frank K. Wilhelm, "Simple pulses for elimination of leakage in weakly nonlinear qubits," Phys. Rev. Lett. **103**, 110501 (2009).

[41] Romeo Bianchetti, Stefan Filipp, Matthias Baur, Johannes M. Fink, Christian Lang, Lars Steffen, Maxime Boissonneault, Alexandre Blais, and Andreas Wallraff, "Control and tomography of a three level superconducting artificial atom," Phys. Rev. Lett. **105**, 223601 (2010).

[42] Marek Pechal, Lukas Huthmacher, Christopher Eichler, Sina Zeytinoglu, Abdufarrukh A. Abdumalikov, Simon Berger, Andreas Wallraff, and Stefan Filipp, "Microwave-controlled generation of shaped single photons in circuit quantum electrodynamics," Phys. Rev. X **4**, 041010 (2014).

[43] Michael Fleischhauer and Aaron S. Manka, "Propagation of laser pulses and coherent population transfer in dissipative three-level systems: An adiabatic dressed-state picture," Phys. Rev. A **54**, 794–803 (1996).

[44] David C. McKay, Christopher J. Wood, Sarah Sheldon, Jerry M. Chow, and Jay M. Gambetta, "Efficient Z gates for quantum computing," Phys. Rev. A **96**, 022330 (2017).

[45] J. Robert Johansson, Paul D. Nation, and Franco Nori, "Qutip 2: A python framework for the dynamics of open quantum systems," Comput. Phys. Commun. **184**, 1234 – 1240 (2013).

[46] J. A. Schreier, A. A. Houck, J. Koch, D. I. Schuster, B. R. Johnson, J. M. Chow, J. M. Gambetta, J. Majer, L. Frunzio, M. H. Devoret, S. M. Girvin, and R. J. Schoelkopf, "Suppressing charge noise decoherence in superconducting charge qubits," Phys. Rev. B **77**, 180502 (2008).

[47] P. J. J. O'Malley, R. Babbush, I. D. Kivlichan, J. Romero, J. R. McClean, R. Barends, J. Kelly, P. Roushan, A. Tranter, N. Ding, B. Campbell, Y. Chen, Z. Chen, B. Chiaro, A. Dunsworth, A. G. Fowler, E. Jeffrey, E. Lucero, A. Megrant, J. Y. Mutus, M. Neeley, C. Neill, C. Quintana, D. Sank, A. Vainsencher, J. Wenner, T. C. White, P. V. Coveney, P. J. Love, H. Neven, A. Aspuru-Guzik, and J. M. Martinis, "Scalable Quantum Simulation of Molecular Energies," Phys. Rev. X **6**, 031007 (2016).

[48] Nikolaj Moll, Andreas Fuhrer, Peter Staar, and Ivano Tavernelli, "Optimizing qubit resources for quantum chemistry simulations in second quantization on a quantum computer," J. Phys. A: Math. Theor. **49**, 295301 (2016).

[49] James I. Colless, Vinay V. Ramasesh, Dar Dahlen, Machiel S. Blok, Jarrod R. McClean, Jonathan Carter, Wibe A. de Jong, and Irfan Siddiqi, "Robust determination of molecular spectra on a quantum processor," Phys. Rev. X **8**, 011021 (2018).

[50] Chen Wang, Christopher Axline, Yvonne Y. Gao, Teresa Brecht, Yiwen Chu, Luigi Frunzio, Michel Devoret, and Robert J. Schoelkopf, "Surface participation and dielectric loss in superconducting qubits," Appl. Phys. Lett. **107**, 162601 (2015).

[51] Alberto Peruzzo, Jarrod R. McClean, Pete Shadbolt, Man-Hong Yung, Xiao-Qi Zhou, Peter J. Love, Alan Aspuru-Guzik, and Jeremy L. O'Brien, "A variational eigenvalue solver on a photonic quantum processor," Nat. Commun. **5**, 4213 (2014).

[52] P. B. Lanyon, J. D. Whitfield, G. G. Gillett, M. E. Goggin, M. P. Almeida, I. Kassal, J. D. Biamonte, M. Mohseni, B. J. Powell, M. Barbieri, A. Aspuru-Guzik, and A. G. White, "Towards quantum chemistry on a quantum computer," Nat. Chem. **2**, 106–111 (2010).

[53] Jiangfeng Du, Nanyang Xu, Xinhua Peng, Pengfei Wang, Sanfeng Wu, and Dawei Lu, "NMR implementation of a molecular hydrogen quantum simulation with adiabatic state preparation," Phys. Rev. Lett. **104**, 030502 (2010).

[54] Abhinav Kandala, Antonio Mezzacapo, Kristan Temme, Maika Takita, Markus Brink, Jerry M. Chow, and Jay M. Gambetta, "Hardware-efficient quantum optimizer for small molecules and quantum magnets," Nature **549**, 242–246 (2017).

[55] Abhinav Kandala, Kristan Temme, Antonio D. Corcoles, Antonio Mezzacapo, Jerry Chow, and Jay M. Gambetta, "Extending the computational reach of a noisy superconducting quantum processor," arxiv:1805.04492 (2018).

[56] J. Wenner, R. Barends, R. C. Bialczak, Y. Chen, J. Kelly, E. Lucero, M. Mariantoni, A. Megrant, P. J. J. O'Malley, D. Sank, A. Vainsencher, H. Wang, T. C. White, Y. Yin, J. Zhao, A. N. Cleland, and J. M. Martinis, "Surface loss simulations of superconducting coplanar waveguide resonators," Appl. Phys. Lett. **99**, 113513 (2011).

[57] Zhuo-Ping Hong, Bao-Jie Liu, Jia-Qi Cai, Xin-Ding Zhang, Yong Hu, Zidan Wang, and Zheng-Yuan Xue, "Implementing universal nonadiabatic holonomic quantum gates with transmons," Phys. Rev. A **97**, 022332 (2018).

[58] S. J. Glaser, U. Boscain, T. Calarco, C. P. Koch, W. Köckenberger, R. Kosloff, I. Kuprov, B. Luy, S. Schirmer, T. Schulte-Herbrüggen, D. Sugny, and F. K. Wilhelm, "Training schrödinger's cat: quantum optimal control," Eur. Phys. J. D **69**, 279 (2015).

[59] Shai Machnes, Elie Assémat, David Tannor, and Frank K. Wilhelm, "Tunable, flexible, and efficient optimization of control pulses for practical qubits," Phys. Rev. Lett. **120**, 150401 (2018).

[60] Daniel J. Egger and Frank K. Wilhelm, "Optimized controlled z gates for two superconducting qubits coupled through a resonator," Supercond. Sci. Technol. **27**, 014001 (2014).

[61] Daniel J. Egger and Frank K. Wilhelm, "Adaptive hybrid optimal quantum control for imprecisely characterized systems," Phys. Rev. Lett. **112**, 240503 (2014).